Effect of surface wettability on evaporation rate of droplet array

M. Mohib Ur Rehman[1], Alexandros Askounis[2], Gyoko Nagayama (長山 暁子)[3, a)]

[1] Graduate School of Engineering, Kyushu Institute of Technology, Kitakyushu, Fukuoka 804-8550, Japan

[2] School of Engineering, University of East Anglia, Norwich NR4 7TJ, United Kingdom

[3] Department of Mechanical Engineering, Kyushu Institute of Technology, Kitakyushu, Fukuoka 804-8550, Japan

Corresponding Author:

Gyoko Nagayama

Email: nagayama.gyoko725@mail.kyutech.jp

ABSTRACT

The evaporation of droplets in an array is hindered by adjacent droplets because of vapor-mediated interactions. Existing theoretical models for predicting the evaporation rate of droplets in the array neglect the important factor of surface wettability. In this work, we developed a model involving a contact angle function to accurately predict the evaporation rate of droplets with an arbitrary contact angle in the array. Fick's first and second laws were solved for evaporating droplets in the array by using steady-state three-dimensional numerical simulations, to derive the contact angle function. The proposed model was experimentally validated for arrayed droplets evaporating on flat hydrophilic and hydrophobic surfaces. We show that the contact angle function approaches unity on hydrophilic surfaces, which implies that the proposed model coincides with Wray *et al.*'s model. On the other hand, the contact angle function is much lower than unity on hydrophobic surfaces, indicating a low evaporation rate of droplets in the array. The findings of this study are expected to advance our understanding of droplet evaporation in arrays in a wide range of scientific and engineering applications.

I. INTRODUCTION

The evaporation of a single isolated droplet on a solid surface has been extensively studied for basic scientific understanding.[1–9] However, in practice, droplets in arrays are surrounded by adjacent droplets, for instance, in inkjet printing,[10] spray cooling,[11] perspiration on human skin,[12] and DNA mapping,[13] which affects their evaporation kinetics. The recent COVID-19 pandemic highlighted the need to understand the evaporation of multiple virus-laden droplets on different surfaces for predicting virus survival.[14–16] In these applications, the vapor density near the liquid–vapor (lv) interface of a droplet in the array increases when adjacent droplets are present.[17] Local vapor accumulation around the droplet reduces the evaporation rate, prolonging its evaporation time compared with an isolated droplet under identical conditions.[18] This phenomenon is called "shielding effect," owing to the analogy between the vapor cloud in mass transfer and the electronic cloud in quantum mechanics.[19]

Current diffusion-based theoretical models can accurately predict the evaporation rate of an isolated droplet on a flat surface.[20–23] However, in identical conditions, these models overestimate the evaporation rate of a droplet surrounded by neighboring droplets in an array.[24] In this context, Carrier *et al.* introduced the concept of "super-droplet" and proposed an analytical expression that describes how its evaporation is hindered by the presence of adjacent droplets.[25] A basic assumption of this model is that an array of droplets with an arbitrary contact angle can be considered as a single flat super-droplet. However, this assumption prevents the model from accurately predicting the evaporation rate when the distance between individual droplets in the array is larger than a threshold value.[26] To address this limitation, Wray *et al.*[27] proposed a theoretical model by assuming that droplets in the array interact only in the gas domain through diffusion. Wray *et al.*'s model is capable of considering the relative size and position of each droplet in the array to accurately predict the evaporation rate of droplets.[27] Their predictions were experimentally validated by Edwards *et al.*,[28] who used an

interferometric technique to directly measure the individual evaporation rate of droplets on hydrophilic glass surfaces for ten different array configurations.

However, Wray *et al.*'s model[27] is applicable only to droplets on hydrophilic surfaces (so-called thin droplets) in the array. Therefore, the model is inappropriate to predict the evaporation rates of droplets in arrays on hydrophobic surfaces.[29,30] In this study, we propose a generalized model that considers the important factor of surface wettability for accurately predicting the evaporation rate of droplets in array.

II. PROBLEM DESCRIPTION AND THEORETICAL MODELING

An array of N water droplets is considered to evaporate on flat hydrophilic and hydrophobic surfaces. The central droplet of the array is considered as the reference droplet, and it can be surrounded by n_d (1–4) adjacent droplets in different configurations, as shown in Fig. 1. The reference droplet is separated from its adjacent droplets by a constant distance d_s [mm] that ranges from 0 to 80 R_d, where R_d [mm] is the contact radius of the reference droplet. All the droplets in the array have identical R_d and identical contact angle θ. The ambient temperature T and relative humidity RH are maintained constant at 25℃ and 40%, respectively. Vapor continuously diffuses from the lv interface with saturation density ρ_s [g/m^3] to the ambient with density ρ_∞. The external and internal flows in the liquid and gas regimes, respectively, are considered too weak to influence the evaporation rate.[31,32] Furthermore, the effect of gravity on the shape of the droplets is negligible since R_d is smaller than the capillary length (sessile droplets).[33] For an isolated droplet with an arbitrary contact angle evaporating on a flat surface, the instantaneous evaporation rate $\dot{m}_{iso}$ [kg/s] is given by[20]

$$\dot{m}_{iso} = -2\pi R_d D(T)(\rho_s - \rho_\infty)\frac{1}{\sqrt{1+\cos\theta}}, \quad (1)$$

where the diffusion coefficient $D(T)$ =22.5×10^{-6}(T/273.15)$^{1.8}$[m^2/s].[34] The vapor density ρ_s at the lv interface is considered to be saturated at ambient temperature T and is calculated as

$\rho_s(T) = MP_s(T)/R_gT$, where $P_s(T)$ [Pa] is the saturated partial vapor pressure, M [kg/mol] is the vapor molecular weight, and R_g [J/(mol·K)] is the universal gas constant. The ambient density corresponding to relative humidity RH is calculated using $\rho_\infty = RH \times \rho_s(T)$.

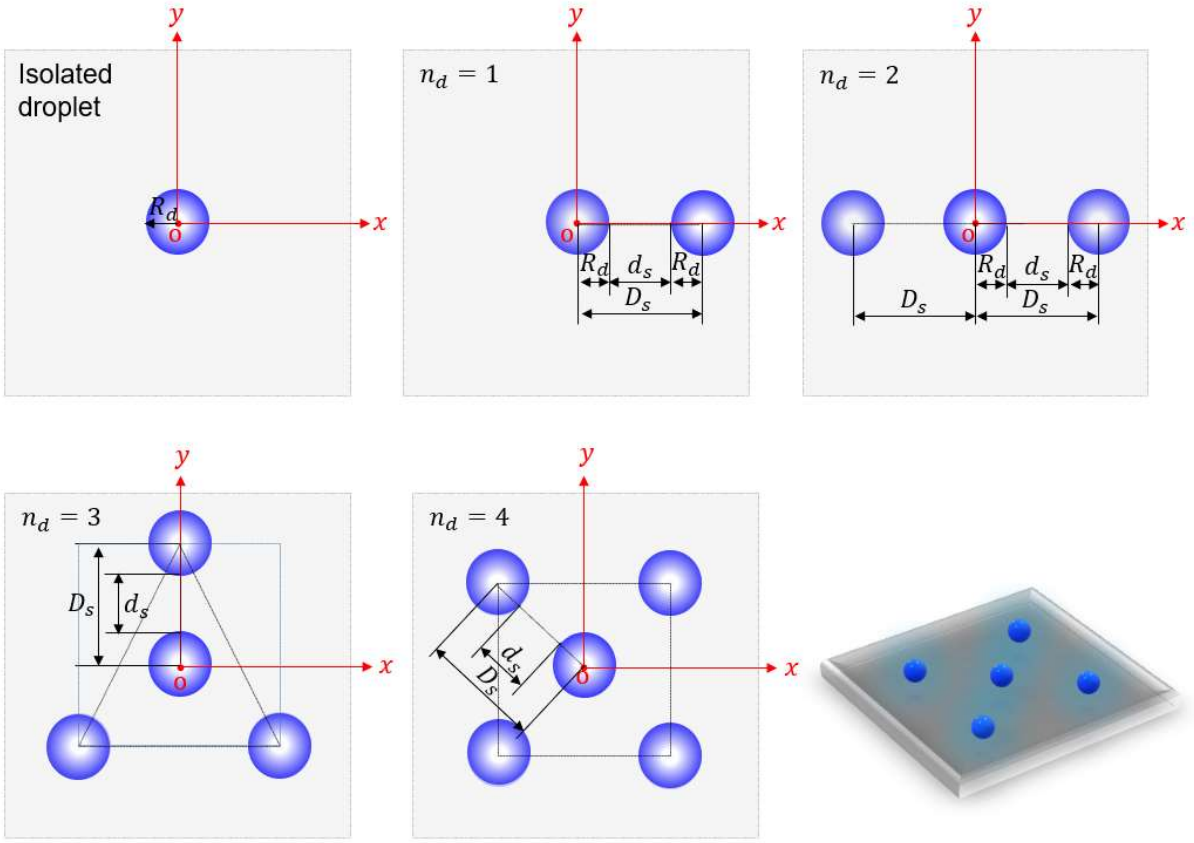

FIG. 1. Schematics of droplet array configurations. The origin of the co-ordinate system is located at center of the reference droplet.

For a reference droplet surrounded by n_d adjacent droplets, the evaporation rate $\dot{m}_o$ can be calculated using Wray *et al.*'s model:[27]

$$\dot{m}_o = \dot{m}_{iso} - \frac{2}{\pi}\sum_{k=1}^{N} \dot{m}_{ad,k} sin^{-1}\left(\frac{R_d}{D_{s,k}}\right). \quad (2)$$

Here, D_s [mm] is the distance between the centers of two adjacent droplets in the array, and it is given by $D_s = d_s + 2R_d$ as shown in Fig. 1; $\dot{m}_{ad}$ is the evaporation rate of adjacent droplets, and k is the number of individual droplets in the array range from 1 to N (total number of droplets). The evaporation rates $\dot{m}_o$ and $\dot{m}_{ad}$ are analogous to the evaporation flux $\dot{m}/A_{lv}$

because the surface area of the lv interface, given by $A_{lv} = 2\pi {R_d}^2/(1 + cos\theta)$ [mm^2], is identical for all the droplets. However, $\dot{m}_o$ and $\dot{m}_{ad}$ are unknown and depend on vapor interactions between the droplets. Therefore, Eq. (2) is a system of $N \times N$ linear equations that should be solved simultaneously. To simplify Eq. (2), Edwards *et al.*[28] rewrote the system of equations in a square matrix as follows:

$$\dot{m}_o = \emptyset^{-1}\dot{m}_{iso}, \tag{3}$$

where $\emptyset$ is an $N \times N$ suppression matrix. The off-diagonal elements capturing the interactions between droplets can be calculated as $\emptyset_{ij} = \frac{2}{\pi} sin^{-1}\left(\frac{R_d}{D_{s,ij}}\right)$; the diagonal elements represent the interaction of a droplet with itself and hence are one. Here, the subscripts *i* and *j* represent the row and column of the suppression matrix $\emptyset$. For the prediction of the evaporation rate of reference droplet $\dot{m}_o$ in Eq. (3), the suppression matrix $\emptyset$ can be reduced to the order $1 \times N$. Matrix $\dot{m}_{iso}$ has an order of $N \times 1$ and contains constants. Further information about the model can be found in the supplementary material of Edwards *et al.*[28] Since the effect of surface wettability is ignored in Eq. (3), we propose a contact angle function $f(\theta)$ to improve Wray *et al.*'s model as follows:

$$\dot{m}_o = \emptyset^{-1}\dot{m}_{iso} f(\theta). \tag{4}$$

Here, $f(\theta)$ was obtained through three-dimensional numerical simulations by solving Fick's first and second laws for steady-state mass transfer.

III. SIMULATION SYSTEM

In the simulation system, only the lv interface of the droplet was considered as the solid–liquid–vapor (slv) interface near the contact line can be ignored for flat surfaces.[35] The droplet evaporation could be considered in a quasi-steady state because the time required for the vapor density to adapt to changes in the droplet shape is of the order of $R_d{}^2/D$.[22] The droplet's shape was assumed to be constant in the simulation system, and the evaporation rate was a function

of R_d and θ at a given instance under ambient conditions.[22] A cylinder with a radius and height of 100 R_d, with $R_d = 1$ mm, was used as the simulation domain, as depicted in Fig. 2(a), and it enclosed a droplet array on a surface located at the bottom of the system. A non-structured tetrahedral grid was used for the spatial discretization of the simulation domain, and the total number of grid elements ranged between 1 and 3 million. Figure 2(b) shows the grid in the *xy*-plane of the simulation domain, and Fig. 2(c) shows an enlarged view of the grid in the vicinity of the droplet array. The element size of the simulation grid was refined in the vicinity of the lv interface of the droplets to improve the simulation accuracy. Simulation grids were generated using the preprocessor SALOME,[36] and the maximum aspect ratio and skewness of the tetrahedral elements in them were below 5 and 0.85, respectively. Thus, it was ensured that the grid quality was not compromised by the presence of a sharp curvature at the lv interface of the droplets in the simulation domain. Only the vapor diffusion from the lv interface to the gas domain was simulated, and the internal flow of the droplet was ignored because the liquid was not included in the simulation domain.

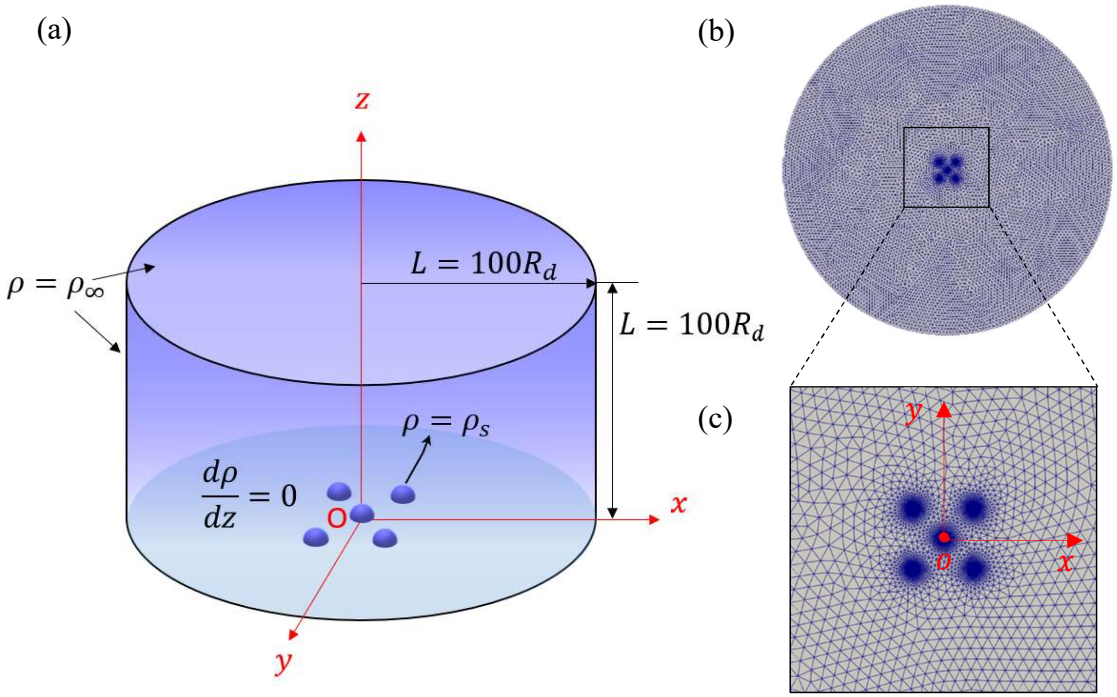

FIG. 2. Simulation system: (a) the domain with boundary conditions, (b) the grid in the *xy*-plane of the simulation domain, and (c) an enlarged view of the grid in the vicinity of the droplet array.

Fick's second law can be written as a three-dimensional Laplace equation in terms of the vapor density ρ:[37]

$$\frac{d^2\rho}{dx^2}+\frac{d^2\rho}{dy^2}+\frac{d^2\rho}{dz^2}=0. \tag{5}$$

The mass transfer rate based on Fick's first law can be written as

$$\dot{m}=-A_{lv}D(T)\left.\frac{d\rho}{dn}\right|_{lv}. \tag{6}$$

Here, $\frac{d\rho}{dn}$ [kg/m^4] is the vapor density gradient normal to the lv interface, and $\hat{n}$ is a unit vector normal to the lv interface.

The cylindrical system was adopted for simplicity, and is shown in Fig. 2(a). The boundary conditions were as follows: (1) at the lv interface of the droplet, the saturated vapor density ρ_s was $23 g/m^3$ at the ambient temperature T=25℃; (2) at the top and side boundaries connected to an air–vapor mixture in the far field, the ambient vapor density ρ_∞ was $9 g/m^3$ at $RH = 40\%$; and (3) at the bottom wall, we considered $d\rho/dz = 0$ since there was no vapor penetration into the wall. The contact angle of all the droplets was identical and in the range of 10° to 170°, and the number of adjacent droplets n_d varied between 0 and 4. The separation distance d_s ranged from R_d to $80R_d$.

TABLE I. Grid size independence for isolated and reference droplets for $\theta = 90^\circ$.

Grid type	Grid size [$\times 10^6$ tetrahedrons]	Evaporation rate -$\dot{m}$ [$\times 10^{-9} kg/s$]	
		Isolated droplet	Reference droplet ($n_d = 4$, $d_s/R_d = 10$)
Coarse	0.1	1.5	1.2
Medium	0.72	2.0	1.6

Fine	1.2	2.3	1.7
Very fine	2.8	2.3	1.7

TABLE II. Domain size independence for isolated and reference droplets for $\theta = 90^{\circ}$.

Domain type	Domain size L [$\times R_d$ mm]	Evaporation rate -$\dot{m}$ [$\times 10^{-9} kg/s$]	
		Isolated droplet	Reference droplet ($n_d = 4\,, d_s/R_d = 10$)
Small	5	2.7	2.2
Medium	50	2.4	1.8
Large	100	2.3	1.7
Very large	150	2.3	1.7

The grid and domain independence were confirmed for all simulations, and the main results are summarized in Tables I and II. Four different grid sizes (i.e., coarse, medium, fine, and very fine) and four different domain sizes (i.e., small, medium, large, and very large) were considered in the analysis. For all simulations, the fine grid type and large domain were chosen to obtain accurate results (see Tables I and II). The edge size of the simulation cell (i.e., the tetrahedron) varied between $0.2R_d$ and $0.002R_d$ across the domain for the fine grid type, and the size of the large domain was fixed at $100R_d$. Further increasing the grid and domain size had no significant effect on the simulation results. The governing equations, Eqs. (5) and (6), were solved using the finite volume method in OpenFOAM.[38] The Gauss linear scheme was adopted as the Laplacian scheme for discretization, and surface normal gradients were corrected. The simulation results were visualized using the post-processor ParaView.[39]

IV. EXPERIMENTAL MATERIALS AND METHODS

An untreated cover glass of 24 mm × 24 mm (Matsunami Glass) with a Young contact angle (static) θ_Y of $50° \pm 2°$ was used as a hydrophilic surface. Hydrophobic surfaces with $\theta_Y = 120° \pm 3°$ were prepared by spraying a commercial water-repellent coating (FK super water-

repellent) evenly onto the cover glass and drying the sprayed glass in a draft chamber for 60 min. A scanning probe microscope (SPM, Shimadzu, SPM-9700HT) was used to observe the surface morphologies of the hydrophilic and hydrophobic surfaces, and images obtained with it are shown in Fig. 3. The average surface roughness *Ra* [nm] was found to be 0.75 ± 0.43 nm for hydrophilic surfaces and 231 ± 87 nm for hydrophobic surfaces. Since *Ra* of both hydrophilic and hydrophobic surfaces was on the nanometer scale, the surfaces were considered to be flat surfaces.

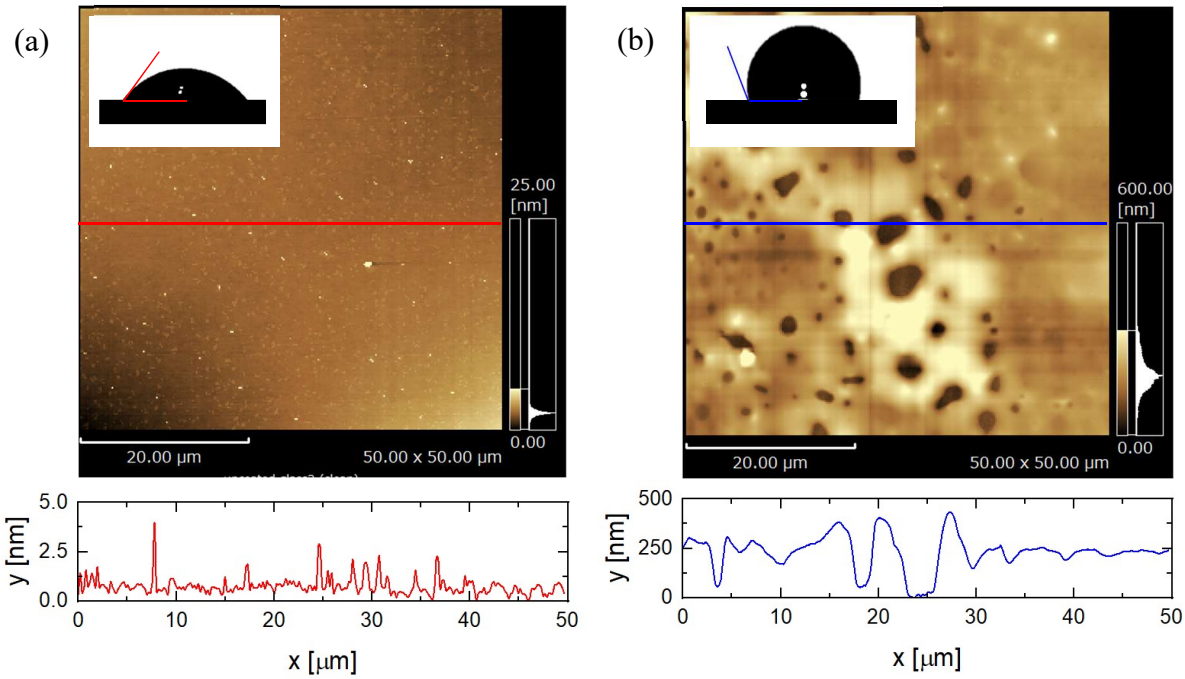

FIG. 3. SPM images and cross-sectional profiles of (a) hydrophilic and (b) hydrophobic surfaces. The insets show Young contact angles (static) at the flat surfaces.

A detailed schematic of the experimental setup is presented in Fig. 4. Deposition positions for the droplet array were manually marked on the rear side of the transparent cover glass, and 1 µL pure water droplets were carefully deposited on the marks with a micropipette (Hamilton, 701 RN), with the aid of a vertically aligned microscope (Sightron, nano capture SP725S). The number of adjacent droplets n_d was set to four, and the separation distance was 10 R_d. The droplets in the array were allowed to evaporate naturally in a measurement cell under controlled

ambient conditions in an environmental chamber (Espec, TBL-4HWOP3A). The measurement cell was made of transparent acrylic to prevent convection around the droplets during evaporation. The dynamics of the reference droplet was recorded using a horizontally oriented digital microscope (Keyence, VHX-200) with a backlight source. The contact angle, contact radius, and volume of the reference droplet were then calculated from recorded videos using an open-source image analysis code (ImageJ, v-1.53)[40]. A thermo recorder (T&D Corporation, TR-72Ui) was used to measure the temperature and relative humidity in the measurement cell during droplet evaporation. Experiments were repeated five times for each measurement of isolated droplets and the reference droplet in arrays on hydrophilic and hydrophobic surfaces. The uncertainty of the results was calculated using the mean and standard deviation of the experimental dataset.

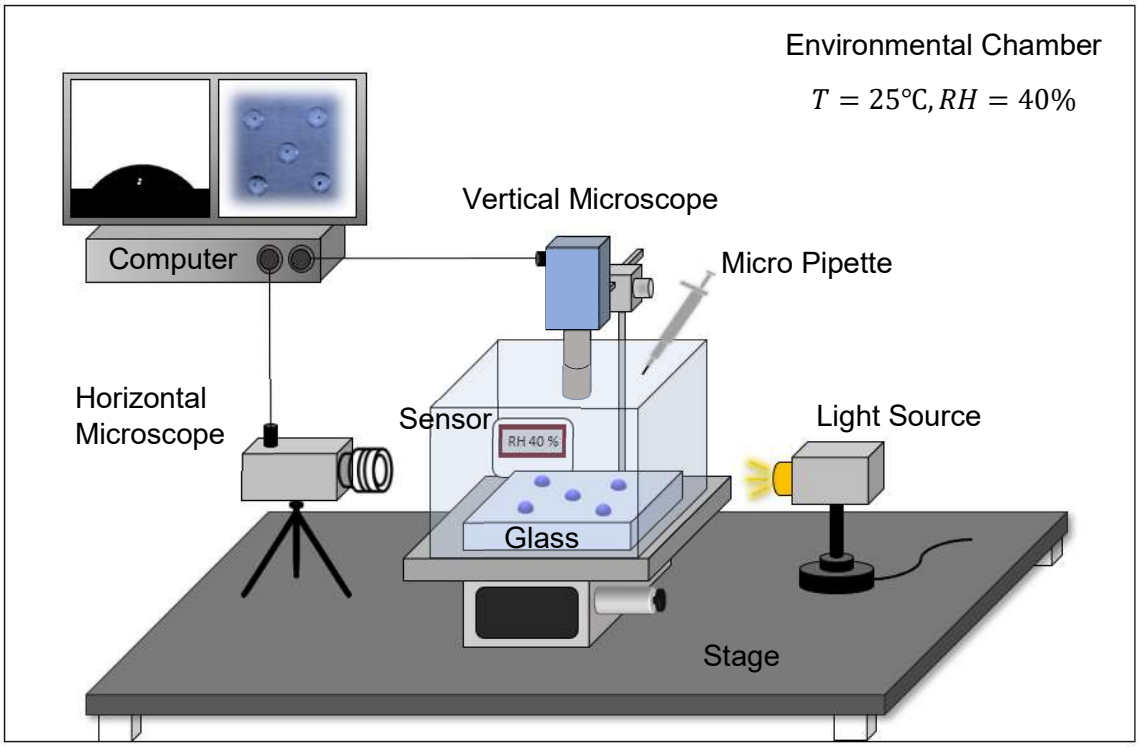

FIG. 4. Schematic of the measurement system used for the evaporation of a droplet array under constant temperature and humidity.

V. RESULTS AND DISCUSSION

The vapor density distribution in the *xy*-plane at the bottom of the simulation domain is shown in Fig. 5, and the normalized local vapor density along the *z*-axis is shown in Fig. 6. For a given contact angle θ, an increase in the number of adjacent droplets n_d increased the vapor density near the reference droplet, thereby suppressing the reference droplet's evaporation rate. For a given n_d, the vapor density near the reference droplet increased significantly as the contact angle increased. This implies that the vapor density profiles in the diffusion domain depended on the surface wettability.

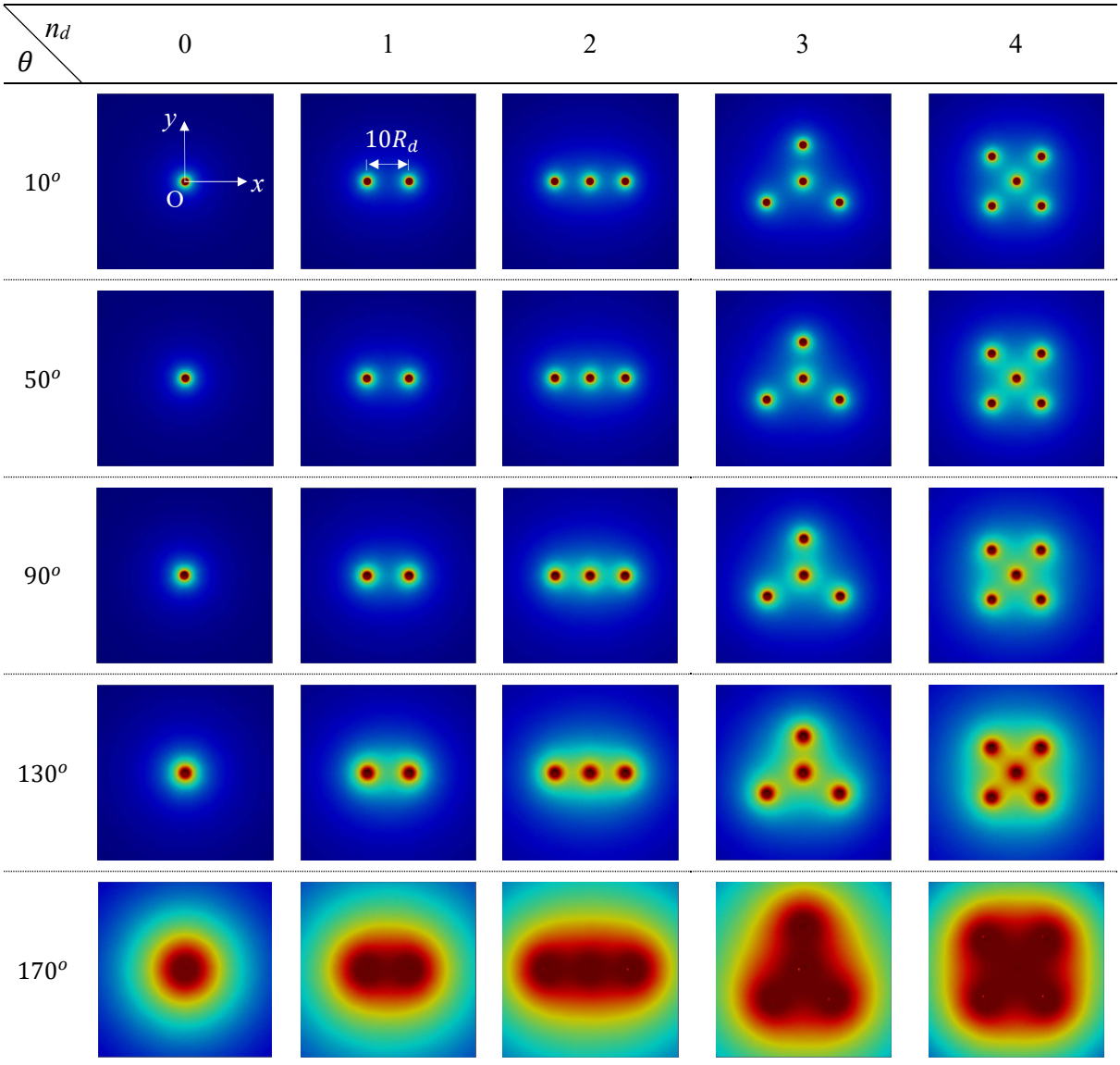

(a)

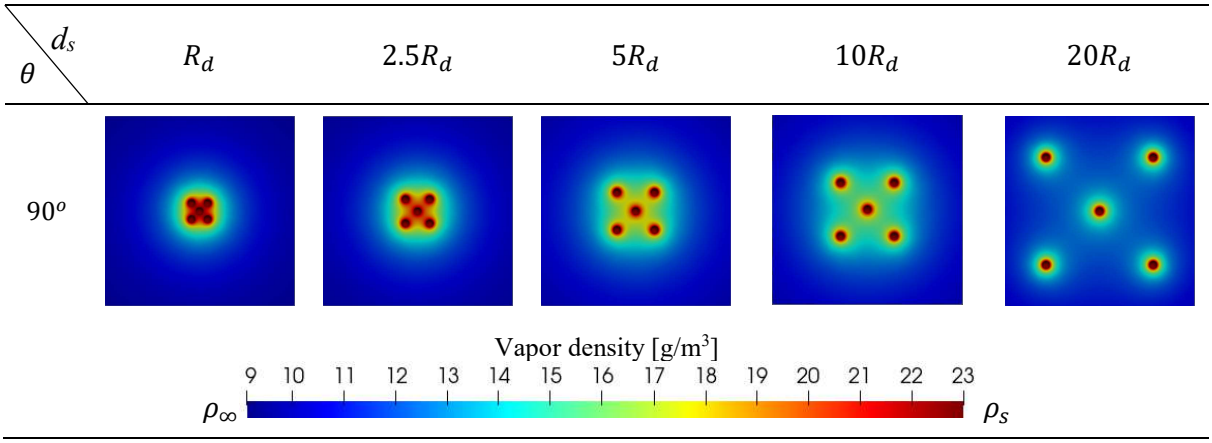

(b)

FIG. 5. Vapor density distribution in the *xy*-plane at the bottom of the simulation domain: (a) effect of contact angle θ and number of adjacent droplets n_d for $d_s = 10\ R_d$, where $R_d = 1mm$, and (b) effect of separation distance d_s for $\theta = 90^o$.

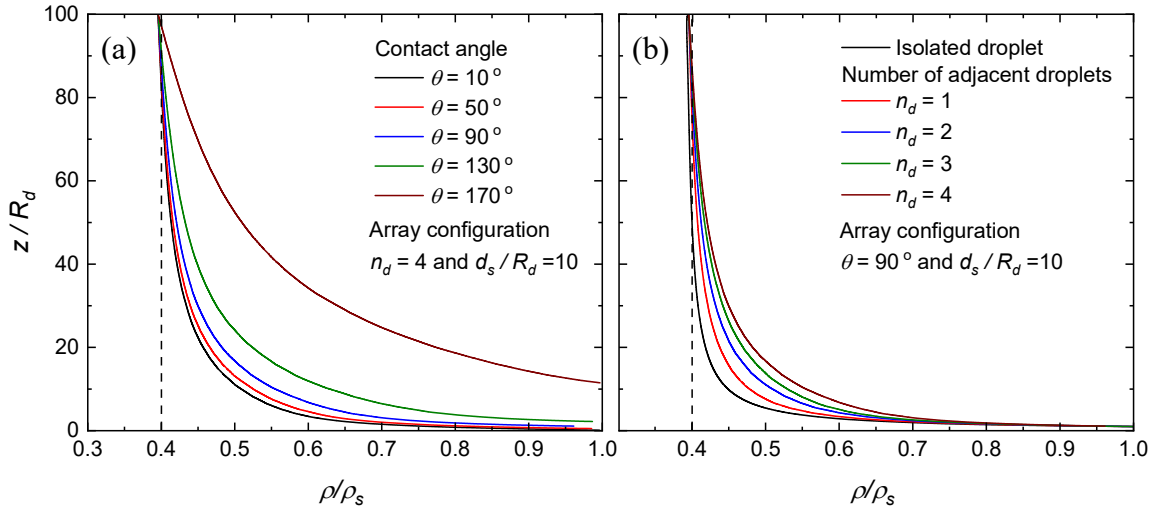

FIG. 6. Normalized vapor density along the *z*-axis for droplet evaporation in an array for (a) different contact angles and (b) different numbers of adjacent droplets. The dotted lines represent *RH*=40%.

Figure 7 shows the relationships between the contact angle, dimensionless separation distance d_s/R_d, and the evaporation rate of the reference droplet ($n_d = 4$). In Fig. 7(a), the normalized evaporation rate $\dot{m}_0/\dot{m}_{iso}$ (based on Eq. 4) of the reference droplet is plotted against d_s/R_d in the contact angle range 10°–170°. A value of one for the ratio $\dot{m}_0/\dot{m}_{iso}$ (dashed line) indicates that the reference droplet's evaporation rate was identical to that of the

isolated droplet under identical conditions. Notably, the larger the contact angle of the isolated droplet, the greater was the value of $\dot{m}_{is}$. On one hand, $\dot{m}_0/\dot{m}_{is}$ significantly decreased with a decrease in d_s/R_d, showing that the separation distance was the primary factor in the reduction of the evaporation rate of droplet arrays. As shown in Fig. 5(b), the local vapor density near the reference droplet relatively increased in the presence of adjacent droplets when the separation distance decreased. Apparently, an extended saturated vapor cloud surrounding the reference droplet hindered vapor diffusion in the computation domain, resulting in the reduction of $\dot{m}_0/\dot{m}_{is0}$ irrespective of the contact angle. As the separation distance increased, $\dot{m}_0/\dot{m}_{is0}$ approached unity, and the reference droplet's evaporation resembled that of an isolated droplet. On the other hand, the dependence of $\dot{m}_0/\dot{m}_{is}$ on the contact angle can be readily discerned in Fig. 7(a), showing that the contact angle was a secondary factor influencing the evaporation rate of droplet arrays. In particular, deviations of $\dot{m}_0/\dot{m}_{is}$ from unity became significant as the contact angle increased. This is because the area of the saturated vapor cloud surrounding the reference droplet increased with the contact angle, as shown in Fig. 6(a) (right most column of n_d = 4). It was found that $\dot{m}_0/\dot{m}_{is0}$ was close to unity at $d_s/R_d = 80$ for the cases with $\theta \leq 130^{\circ}$, and a longer separation distance was required for $\theta = 170^{\circ}$. Thus, the separation distance and contact angle are correlated factors that have a synergetic effect on $\dot{m}_0/\dot{m}_{is0}$.

Wray *et al.'s* model (Eqs. (2) and (3)) plotted in Fig. 7(a) (black line) overlapped with the present numerical results for $\theta = 10^{\circ}$ (black circle) and 50° (red circle), while it deviated from the numerical results for hydrophobic case, $\theta \geq 90^{\circ}$, especially in the region of small separation distances. Although we verified that Wray *et al.*'s model[27] is applicable to the hydrophilic droplets in the array, apparently, this model could not capture the effect of the contact angle on the evaporation rate. Since Fig. 7(a) shows the importance of surface

wettability for predicting the evaporation rate of droplets in the array, surface wettability was incorporated into *f(θ)*, as shown in Eq. (4).

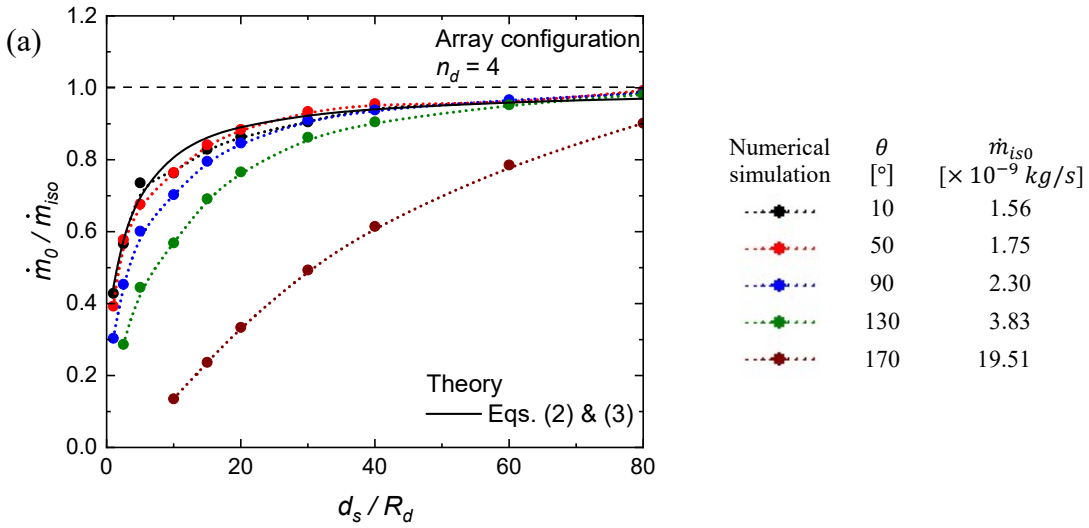

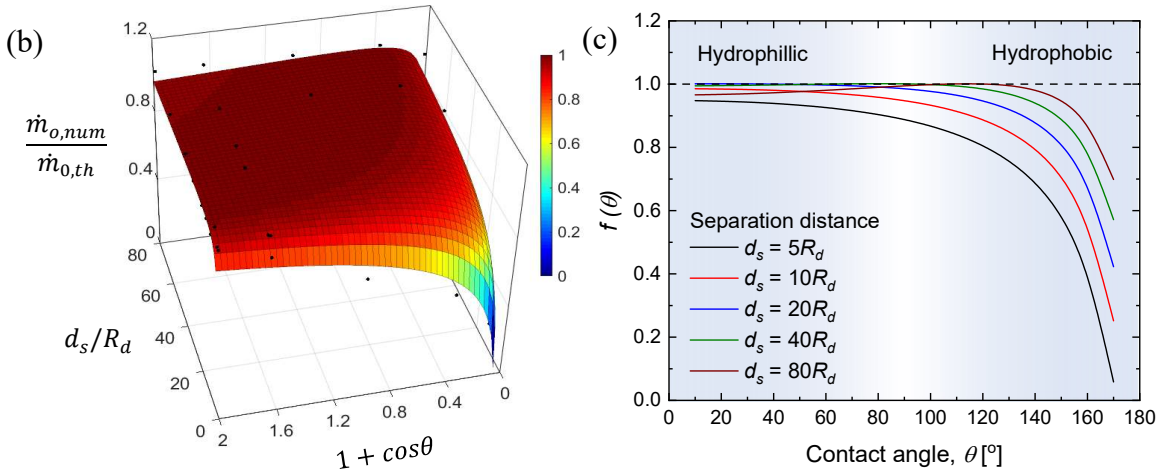

FIG. 7. Effect of the contact angle and dimensionless separation distance d_s/R_d on (a) the evaporation rate of the reference droplet normalized by the evaporation rate of the isolated droplet $\dot{m}_0/\dot{m}_{is0}$, (b) the evaporation rate of the reference droplet normalized by the prediction of Eq. (3) $\dot{m}_{0,num}/\dot{m}_{0,th}$, and (c) the contact angle function $f(\theta)$.

To obtain $f(\theta)$, we plotted the numerically determined evaporation rate of the reference droplet normalized by Eq. (3), $\dot{m}_{0,num}/\dot{m}_{0,th}$, against d_s/R_d and $1 + cos\theta$, as shown in Fig. 7(b). Similar to Fig. 7(a), a decrease in the separation distance d_s/R_d and an increase in the

contact angle term $1 + cos\theta$ caused a reduction in $\dot{m}_{0,num}/\dot{m}_{0,th}$. Through MATLAB[41] analysis, $f(\theta)$ was obtained by fitting the dataset in Fig. 7 with a quadratic function as follows:

$$f(\theta) = a + bx + cx^2, \text{ where } x = ln\left[\frac{d_s}{R_d}(1 + cos\theta)\right]. \quad (7)$$

Table III presents the values of coefficients a, b, and c in Eq. (7) for different numbers of adjacent droplets n_d, and the values are valid for the contact angle range $\theta = 10^{\circ}-170^{\circ}$ and for the separation distance range $d_s = R_d-80R_d$. In Fig. 7(c), $f(\theta)$ is plotted as a function of the contact angle and separation distance. For $f(\theta)$ = 1, Wray *et al.*'s model[27] coincides with the present model for the hydrophilic cases. However, $f(\theta)$ apparently decreases for the hydrophobic cases, which should be considered in the prediction of the evaporation rate of a droplet in arrays on hydrophobic surfaces.

TABLE III. Model coefficients for different numbers of adjacent droplets.

Number of adjacent droplets n_d	Model coefficients		
	a	b	c
1	0.900	0.056	-0.008
2	0.800	0.116	-0.016
3	0.710	0.166	-0.022
4	0.670	0.176	-0.023

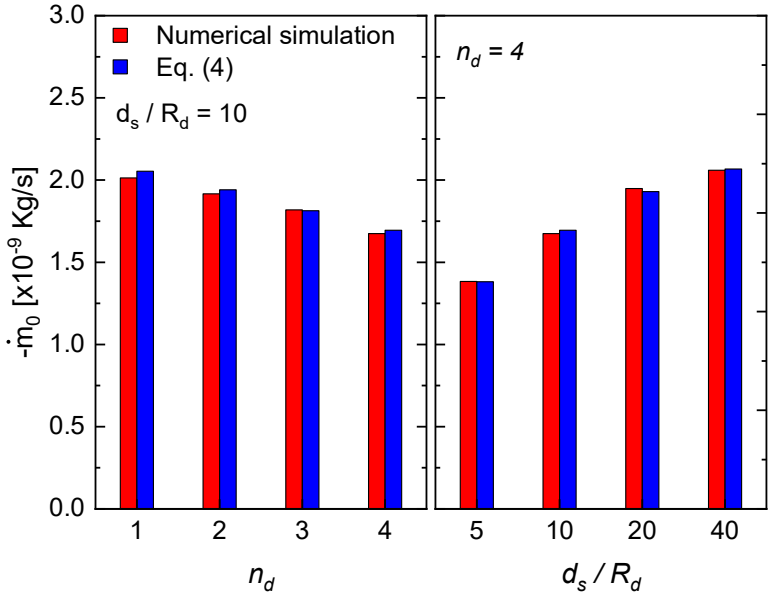

FIG. 8. Model validation for different array configurations. The contact angle of droplets in an array was set to $\theta = 90^{\circ}$.

The $\dot{m}_0$ value predicted by Eq. (4) was compared with the simulation results in Fig. 8, and a good agreement was found for different array configurations for $\theta = 90^{\circ}$. To validate the present model, we performed experiments involving evaporation of droplets in isolation and in arrays on flat hydrophilic and hydrophobic surfaces under identical conditions. The time history of experimental data of the evaporating reference droplet on hydrophilic and hydrophobic surfaces is presented in Fig 9. As shown in Figs. 9(a) and 9(b), temporal variations of the ambient temperature and relative humidity in the measurement cell were small, in the ranges of $T = 25 \pm 2℃$ and $RH = 40 \pm 3\%$. This eliminated the possibility of the ambient conditions influencing the experimental results. Figures 9(c) and 9(d) show that three evaporation modes, namely constant contact radius (CCR), constant contact angle (CCA), and mixed modes, existed for all cases. For hydrophilic surfaces, the evaporation of the isolated droplet was similar to that of the reference droplet in the array, with the CCR mode being dominant. However, for droplet evaporation on hydrophobic surfaces, the contributions of the CCA and mixed modes were significant. Figure 9(c) shows that the CCR mode's duration for the droplet evaporating in the array was longer than that for the isolated droplet. Hydrophobic surfaces showed a longer CCR mode duration than hydrophilic surfaces, because of the slower change of the droplet shape and longer pinning period resulting from the presence of adjacent droplets. Similar results for the durations of the CCA and mixed modes are presented in Fig. 9(d), and they show longer durations of these modes for the reference droplet compared with their durations for the isolated droplet. Figure 9(e) shows the time history of the droplet volume during evaporation. The reference droplet (closed squares) evaporated more slowly than the isolated droplet (open circles), on the same surface under the same ambient conditions. In particular, the reference droplet on a hydrophobic surface (blue) evaporated much slower than

that on a hydrophilic surface (red) for the same array configuration of $n_d = 4$ and $d_s/R_d = 10$. This confirmed our earlier inference from Fig. 7 that the surface wettability should be considered for predicting droplet evaporation in an array.

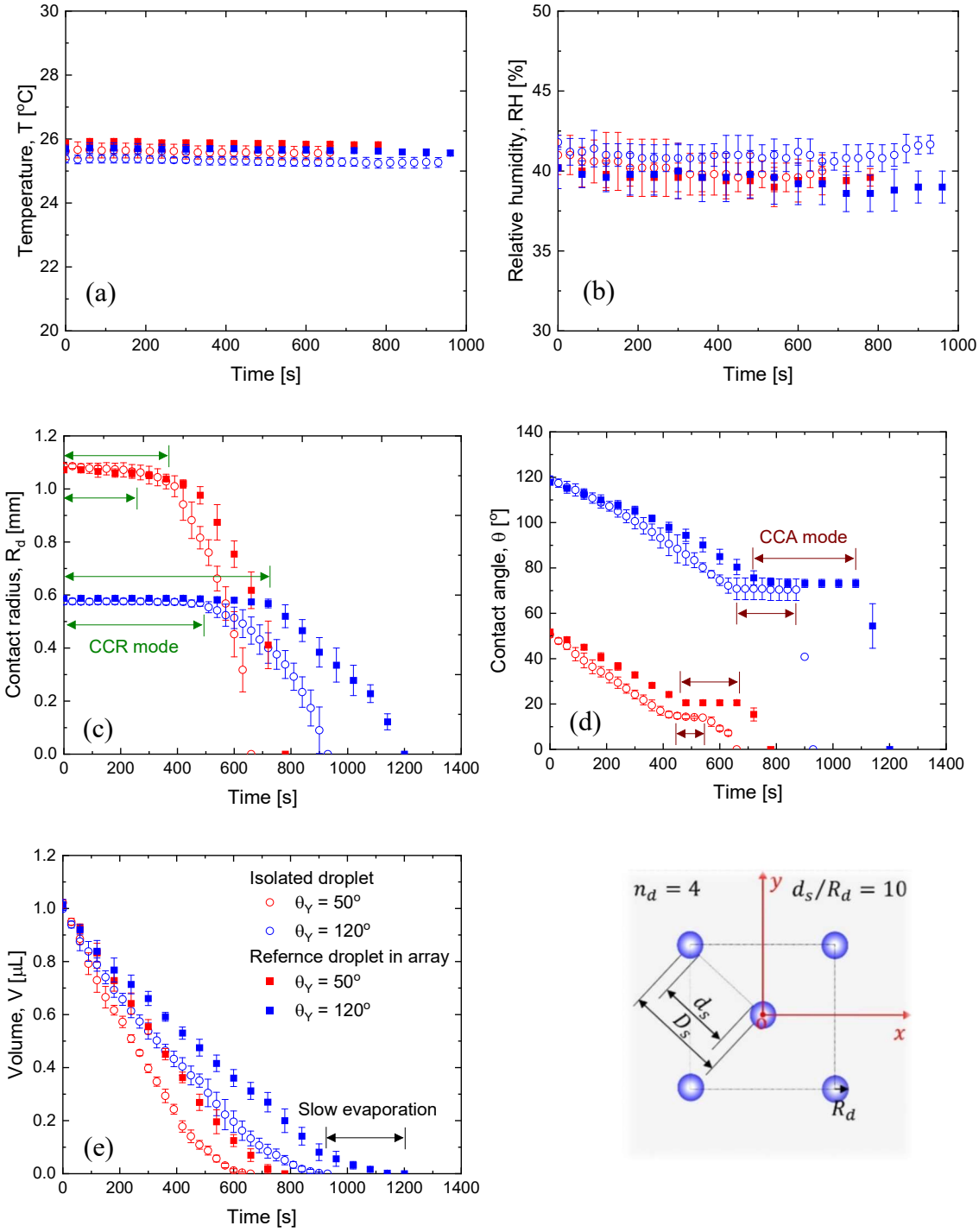

FIG. 9. Temporal variations of the measured (a) temperature, (b) relative humidity, (c) contact radius, (d) contact angle, and (e) droplet volume during droplet evaporation on hydrophilic

($\theta_Y = 50^\circ$, red) and hydrophobic surfaces ($\theta_Y = 120^\circ$, blue) in isolation (open circles) and in arrays (closed squares). The configuration of the droplet array was set to $n_d = 4$ and $d_s/R_d = 10$. Markers in the subfigures are consistent, and their labels correspond to the legend in Fig. 9(e).

In the CCA and CCR modes of evaporation, R_d and θ was reduced from initial values (see Figs. 9(c) and (d)). This decrease caused d_s/R_d to increase and *f(θ)* to be equal to 1. This significantly affected $\dot{m}_0$, as shown in Fig. 7, and was therefore considered in the theoretical prediction based on Eq. (4). The time-dependent *f(θ)* and d_s/R_d were calculated from temporal data of R_d and θ, and they are presented in Fig. 10 for reference droplets evaporating on hydrophilic and hydrophobic surfaces. Figure 10(a) shows that *f(θ)* approached one for both the hydrophilic (red) and hydrophobic (blue) surfaces as the evaporation progressed because of decrease in θ, as shown in Fig. 9(d). However, *f(θ)* was much lower for the hydrophobic surface at the onset of evaporation compared with *f(θ)* for the hydrophilic surface. As time progressed, d_s/R_d increased on both the hydrophilic and hydrophobic surfaces as the R_d of reference droplet decreased during its evaporation in CCA mode. These findings are consistent with the data shown in Fig. 7.

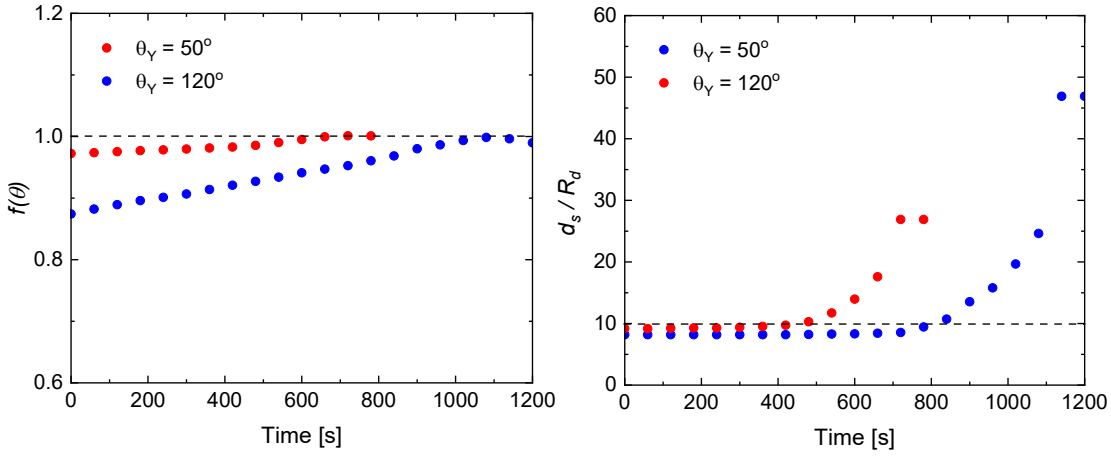

FIG. 10. Temporal evolution of (a) $f(\theta)$ and (b) d_s/R_d during droplet evaporation in arrays on hydrophilic (red) and hydrophobic surfaces (blue). The configuration of the droplet array was set to $n_d = 4$ and $d_s/R_d = 10$.

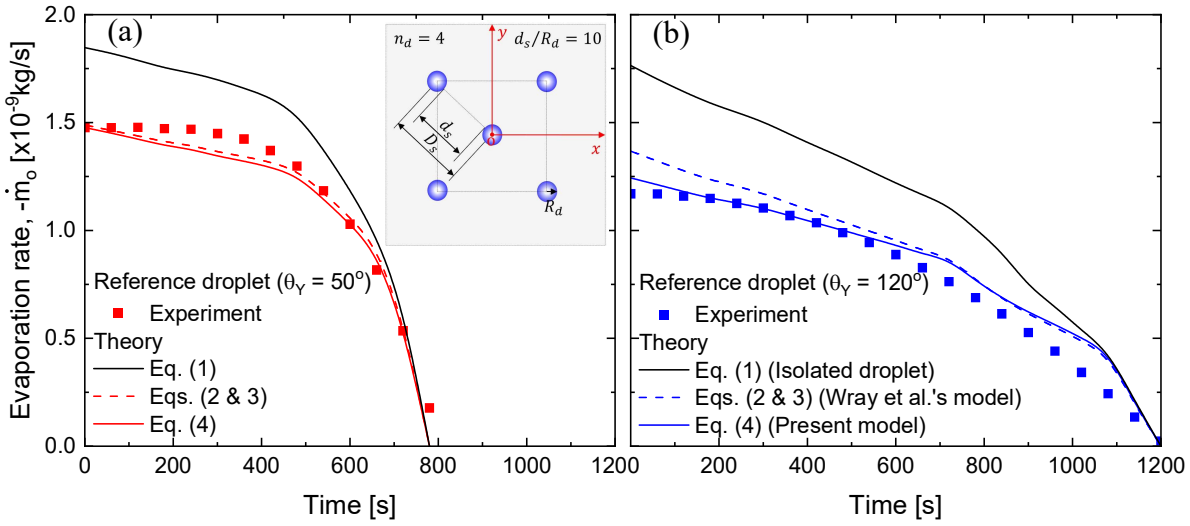

FIG. 11. Theoretical and experimental evaporation rates $\dot{m}_o$ for a reference droplet on (a) hydrophilic and (b) hydrophobic surfaces. The configuration of the droplet array was set to n_d = 4 and d_s/R_d =10.

The mass of the reference droplet during evaporation was first calculated from its measured volume V in Fig. 9(e), and the variation of the droplet mass with time (i.e., gradient) was calculated in MATLAB[41]. Since the calculated gradients were nonlinear, the linearized fitting $\dot{m}_o = p(Sin(t-\pi)) + q(t-10)^2 + 0.95r$ was used to determine $\dot{m}_o$ from experiments. Here, t is the time, and p, q, and r are coefficients determined by curve-fitting the experimental data. A comparison of the experimentally and theoretically obtained $\dot{m}_o$ values is shown in Fig. 11. Since Eq. (1) was proposed for an isolated droplet's evaporation,[14] it overpredicted evaporation rates on hydrophilic and hydrophobic surfaces. As shown in Fig. 11, Eq. (1) deviated significantly from the experimental results at the beginning of evaporation. When *f(θ)* approaches 1 and d_s/R_d increased beyond 10 at the end of evaporation (see Fig.10), the effect of the adjacent droplet on the evaporation of the reference droplet could be ignored. Therefore,

$\dot{m}_0$ predicted by Eq. (4) for the reference droplet agreed with $\dot{m}_{iso}$ predicted by Eq. (1) for the isolated droplet, as shown in Fig. 11. In Fig. 11(a), the present model can be seen to agree well with Wray *et al.*'s model[27] and with the experimental results for the evaporation rate of the reference droplet on a hydrophilic surface. However, as shown in Fig. 11(b), for a hydrophobic surface, the present model does not agree with Wray *et al.*'s model,[27] but shows good agreement with the experimental evaporation rate of the reference droplet. This observation confirms that surface wettability is an important factor influencing droplet evaporation, especially for hydrophobic surfaces.

VI. CONCLUSION

We demonstrate that a droplet in a droplet array evaporates more slowly than an isolated droplet under identical conditions. The reduction on the evaporation rate of the droplet in an array result from the synergetic effect of the separation distance and surface wettability, because of vapor-mediated interactions between droplets. Although the primary factor of the reduction on the evaporation rate is the separation distance, the secondary factor of surface wettability is particularly important for hydrophobic surfaces. The contact angle function introduced in the present model should not be ignored when predicting the evaporation rates of droplets in arrays on hydrophobic surfaces. Since the solid–liquid–vapor (slv) interface also contributes to droplet evaporation,[35] the effect of the slv interface on droplet evaporation in an array will be investigated in a future study. The insights obtained in the present study are expected to pave the way for wider engineering and medical applications of droplet-array-based devices.

ACKNOWLEDGMENTS

This work was supported by the Ministry of Education, Science and Culture of the Japanese Government through the Grant-in Aid for Scientific Research, Project No. 22H01416, and the

Initiative for Realizing Diversity in the Research Environment by Ministry of Education, Culture, Sports, Science and Technology, Japan.

AUTHOR DECLARATIONS

Conflict of Interest

The authors have no conflicts to disclose.

Author Contributions

M. Mohib Ur Rehman: Investigation, Methodology, Data curation, Formal analysis, Writing - original draft. Alexandros Askounis: Conceptualization, Writing - review & editing. Gyoko Nagayama: Conceptualization, Supervision, Writing - review & editing, Funding acquisition.

REFERENCES

[1] X. Yu and J. Xu, Appl. Phys. Lett. **116**, 253903 (2020).
[2] I.G. Hwang, J.Y. Kim, and B.M. Weon, Appl. Phys. Lett. **110**, 31602 (2017).
[3] C.-C. Hsu, T.-W. Su, C.-H. Wu, L.-S. Kuo, and P.-H. Chen, Appl. Phys. Lett. **106**, 141602 (2015).
[4] F. Carle, B. Sobac, and D. Brutin, Appl. Phys. Lett. **102**, 61603 (2013).
[5] L. Bansal, S. Hatte, S. Basu, and S. Chakraborty, Appl. Phys. Lett. **111**, 101601 (2017).
[6] Y. Kita, A. Askounis, M. Kohno, Y. Takata, J. Kim, and K. Sefiane, Appl. Phys. Lett. **109**, 171602 (2016).
[7] A.E. Korenchenko and A.A. Zhukova, Phys. Fluids **34**, 42102 (2022).
[8] A. Paul and P. Dhar, Phys. Fluids **33**, 122010 (2021).
[9] S. Tonini, G.E. Cossali, E.A. Shchepakina, V.A. Sobolev, and S.S. Sazhin, Phys. Fluids **34**, 73312 (2022).
[10] P.M. Theiler, F. Lütolf, and R. Ferrini, Opt. Express **26**, 11934 (2018).
[11] J.D. Benther, J.D. Pelaez-Restrepo, C. Stanley, and G. Rosengarten, Int. J. Heat Mass Transf. **178**, 121587 (2021).
[12] T. Kokalj, H. Cho, M. Jenko, and L.P. Lee, Appl. Phys. Lett. **96**, 163703 (2010).
[13] J. Jing, J. Reed, J. Huang, X. Hu, V. Clarke, J. Edington, D. Housman, T.S. Anantharaman, E.J. Huff, B. Mishra, B. Porter, A. Shenker, E. Wolfson, C. Hiort, R. Kantor, C. Aston, and D.C. Schwartz, Proc. Natl. Acad. Sci. **95**, 8046 (1998).
[14] R. Bhardwaj and A. Agrawal, Phys. Fluids **32**, 61704 (2020).
[15] Z.(贺子龙) He, S.(邵思尧) Shao, J.(李家骐) Li, S.S. Kumar, J.B. Sokoloff, and J.(洪家荣) Hong, Phys. Fluids **33**, 13309 (2021).
[16] S. Chatterjee, J.S. Murallidharan, A. Agrawal, and R. Bhardwaj, Phys. Fluids **33**, 21701 (2021).
[17] S. Hatte, K. Pandey, K. Pandey, S. Chakraborty, and S. Basu, J. Fluid Mech. **866**, 61 (2019).
[18] H. Chen, Q. An, H. Zhang, C. Li, H. Fang, and Z. Yin, Phys. Fluids **34**, 82010 (2022).
[19] F.G.H. Schofield, A.W. Wray, D. Pritchard, and S.K. Wilson, J. Eng. Math. **120**, 89 (2020).
[20] D. Hu, H. Wu, and Z. Liu, Int. J. Therm. Sci. **84**, 300 (2014).

[21] Y.O. Popov, Phys. Rev. E **71**, 36313 (2005).
[22] H. Hu and R.G. Larson, J. Phys. Chem. B **106**, 1334 (2002).
[23] J.M. Stauber, S.K. Wilson, B.R. Duffy, and K. Sefiane, J. Fluid Mech. **744**, R2 (2014).
[24] D.J. Fairhurst, J. Fluid Mech. **934**, F1 (2022).
[25] O. Carrier, N. Shahidzadeh-Bonn, R. Zargar, M. Aytouna, M. Habibi, J. Eggers, and D. Bonn, J. Fluid Mech. **798**, 774 (2016).
[26] K. Pandey, S. Hatte, K. Pandey, S. Chakraborty, and S. Basu, Phys. Rev. E **101**, 43101 (2020).
[27] A.W. Wray, B.R. Duffy, and S.K. Wilson, J. Fluid Mech. **884**, A45 (2020).
[28] A.M.J. Edwards, J. Cater, J.J. Kilbride, P. Le Minter, C. V Brown, D.J. Fairhurst, and F.F. Ouali, Appl. Phys. Lett. **119**, 151601 (2021).
[29] H. Zhang, Y. Kita, D. Zhang, G. Nagayama, Y. Takata, K. Sefiane, and A. Askounis, Heat Transf. Eng. **41**, 1654 (2020).
[30] D. Orejon, K. Sefiane, and M.E.R. Shanahan, Langmuir **27**, 12834 (2011).
[31] M.R. Barmi and C.D. Meinhart, J. Phys. Chem. B **118**, 2414 (2014).
[32] E. Dietrich, S. Wildeman, C.W. Visser, K. Hofhuis, E.S. Kooij, H.J.W. Zandvliet, and D. Lohse, J. Fluid Mech. **794**, 45 (2016).
[33] T.W.G. van der Heijden, A.A. Darhuber, and P. van der Schoot, Langmuir **34**, 12471 (2018).
[34] T.R. Marrero and E.A. Mason, J. Phys. Chem. Ref. Data **1**, 3 (1972).
[35] M.M.U. Rehman and G. Nagayama, Colloids Surfaces A Physicochem. Eng. Asp. **656**, 130419 (2023).
[36] V. Bergeaud and V. Lefebvre, in *Proc. SNA + MC2010 Jt. Int. Conf. Supercomput. Nucl. Appl. + Monte Carlo 2010 Tokyo* (Japan, 2010), p. 1630.
[37] A. Fick, Ann. Phys. **170**, 59 (1855).
[38] H.G. Weller, G. Tabor, H. Jasak, and C. Fureby, Comput. Phys. **12**, 620 (1998).
[39] J.P. Ahrens, B. Geveci, and C.C. Law, in *Vis. Handb.* (2005).
[40] C.A. Schneider, W.S. Rasband, and K.W. Eliceiri, Nat. Methods **9**, 671 (2012).
[41] MATLAB and Statistics Toolbox Release 2012b, The MathWorks, Inc., Natick, Massachusetts, United States.